Article

Electronic Structures of Molecular Beam Epitaxially Grown SnSe2 Thin Films on √3×√3-Sn reconstructed Si(111) surface

Zhujuan Li , Qichao Tian , Kaili Wang , Yuyang Mu , Zhenjie Fan , Xiaodong Qiu , Qinghao Meng , Can Wang , Yi Zhang *

Posted Date: 8 May 2025

doi: 10.20944/preprints202505.0608.v1

Keywords: SnSe2; electronic structures; molecular beam epitaxy; structural phase transition; angle-resolved photoemission spectroscopy

Article

Electronic Structures of Molecular Beam Epitaxially Grown $SnSe_2$ Thin Films on $\sqrt{3} \times \sqrt{3}$-Sn reconstructed Si(111) surface

Zhujuan Li [1,†], Qichao Tian [1,†], Kaili Wang [1], Yuyang Mu [1], Zhenjie Fan [1], Xiaodong Qiu [1], Qinghao Meng [1], Can Wang [1,2,3] and Yi Zhang [1,2,4,5,*]

[1] National Laboratory of Solid State Microstructure, School of Physics, Nanjing University, Nanjing, 210093, China
[2] Collaborative Innovation Center of Advanced Microstructures, Nanjing University, Nanjing, 210093, China
[3] Hunan Provincial Key Laboratory of Flexible Electronic Materials Genome Engineering, School of Physics and Electronic Sciences, Changsha University of Science and Technology, Changsha 410114, China
[4] Jiangsu Physical Science Research Center, Nanjing University, Nanjing, 210093, China
[5] Hefei National Laboratory, Hefei, 230088, China
[†] The authors contributed equally to this work.
[*] Correspondence: zhangyi@nju.edu.cn

Abstract: $SnSe_2$, as a prominent member of post-transition metal dichalcogenides, exhibits many intriguing physical phenomena and excellent thermoelectric properties, calling for both fundamental study and potential application in 2D devices. In this article, we realized the molecular beam epitaxial growth of $SnSe_2$ films on $\sqrt{3} \times \sqrt{3}$-Sn reconstructed Si(111) surface. The analysis of reflection high-energy electron diffraction reveal the in-plane lattice orientation as $SnSe_2$[110]//$\sqrt{3}$-Sn[112]//Si[110]. Besides, the flat morphology of $SnSe_2$ film was identified by scanning tunneling microscopy (STM), implying the relatively strong adsorption effect of $\sqrt{3}$-Sn/Si(111) substrate to the $SnSe_2$ adsorbates. Subsequently, the interfacial charge transfer was observed by X-ray photoemission spectroscopy. Afterwards, the direct characterization of electronic structures was obtained via angle-resolved photoemission spectroscopy. In addition to proving the presence of interfacial charge transfer again, a new relatively flat in-gap band was found in monolayer and few-layer $SnSe_2$, which was disappeared in multi-layer $SnSe_2$. The interface strain induced partial structural phase transition of thin $SnSe_2$ films is presumed to be the reason. Our results provide important information on characterization and effective modulation of electronic structures of $SnSe_2$ grown on $\sqrt{3}$-Sn/Si(111), paving the way for the further study and application of $SnSe_2$ in 2D electronic devices.

Keywords: $SnSe_2$; electronic structures; molecular beam epitaxy; structural phase transition; angle-resolved photoemission spectroscopy

1. Introduction

Post-transition metal dichalcogenides (PTMCs), composed of III-VA metal elements (Ga, In, Sn, Bi, etc) and chalcogen elements (S, Se, Te), is a new class of layered two-dimensional (2D) materials that intrigued extensive studies recently. In addition to the highly anisotropic lattice structure and unique electronic structures, many outstanding electrochemical, thermoelectric, and optoelectronic properties were observed in PTMCs. Therefore, PTMCs have been applied in many fields like electrochemistry [1,2], electronics [3-5], optoelectronics [6,7] and gas sensing [8]. As a prominent member of PTMCs, $SnSe_2$ is an intrinsic layered semiconductor, exhibiting considerable bandgap and excellent thermoelectric properties like ultra-low thermal conductivity and high carrier mobility [9,10]. Together with high abundance and low toxicity of Sn, $SnSe_2$ shows potential applications in optoelectronics [11,12], thermoelectric devices [13], lithium-ion batteries [14] and phase change memory [15].

 doi:10.20944/preprints202505.0608.v1

Besides, intriguing physical properties like charge density wave (CDW), superconductivity, and interfacial polarons were observed in $SnSe_2$ from previous works [16-18]. The interface properties of monolayer (ML) $SnSe_2$ could be effectively tuned by choosing different substrates. For examples, a recent study showed that ML and bilayer $SnSe_2$ films grown on Si(111) undergoes a commensurate CDW transition at $T_C \sim 78$ K driven by Fermi surface nesting between symmetry inequivalent electron pockets, forming a corresponding (2×2) superlattice[18]. In addition, the formation of interfacial polarons induced by charge accumulation and electron-phonon coupling between $SrTiO_3$ and $SnSe_2$ was evidenced [17]. Besides, the superconductivity in $SnSe_2$, which can be modulated by cation intercalation [19] and dielectric gating techniques [20], was reported to be enhanced in the epitaxial $SnSe_2$ on graphitized SiC(0001) substrate [16]. However, there are only a few studies on $SnSe_2$ film grown on Si(111), especially the study on direct characterization of band structures is still lacking. In this paper, we synthesize $SnSe_2$ films on Si(111) by molecular beam epitaxy (MBE), and employ in-situ reflection high energy electron diffraction (RHEED), scanning tunneling microscopy (STM), X-ray photoemission spectroscopic (XPS) and angle-resolved photoemission spectroscopy (ARPES) to characterize the atomic and electronic structures of them. We found that the $SnSe_2$ shows layer-by-layer growth mode on $\sqrt{3}$-Sn/Si(111) substrate with high-quality of flatness. The interfacial charge transfer effect is observed in the $SnSe_2$ film grown on $\sqrt{3}$-Sn/Si(111) substrate. Moreover, an emerging band above the original valence band of bulk $SnSe_2$ is found in the $SnSe_2$ thin film, resulting the reduction of the indirect band gap. This emerging band is suggested to be induced by the interfacial strain driven structural phase transition of the grown $SnSe_2$. Our results provide important information for the further applications of $SnSe_2$ film in 2D electronic devices.

2. Materials and Methods

All the experiments were performed in a combined MBE-STM-ARPES ultra-high vacuum (UHV) system with a base pressure of ~ 2×10^{-10} mbar. At first, to get a clean Si(111)-(7×7) reconstructed surface, a Si(111) substrate (n-doped by P) was initially degassed at 650℃, followed by flash-annealing to ~1250℃ for 20 cycles. To passivate the dangling bonds of Si(111)-(7×7) surface and enhance the surface diffusion for the growth of $SnSe_2$, we evaporated 1/3 monolayer of Sn on Si(111)-(7×7) surface at 550℃, leading to a well-ordered $\sqrt{3} \times \sqrt{3}\,R30°$-Sn recontruction surface on Si(111) ($\sqrt{3}$-Sn/Si(111) in the following) surface. Next, the $SnSe_2$ films were grown by co-depositing high-purity Sn (99.99%) and Se (99.99%) from standard Knudsen cells separately, onto the $\sqrt{3}$-Sn/Si(111) substrate at 200℃. The temperatures of the Sn and Se sources were maintained at 920 ℃ and 130℃, respectively, keeping the flux ratio at Sn:Se ~1:20. During the film growth, an in-situ RHEED was used for real time monitor and surface structural characterization. After growth, the surface morphology was further characterized by an in-situ room-temperature STM (RT-STM). Subsequently, to investigate the electronic structures, the in-situ low temperature (~10 K) XPS and ARPES were performed by a shared DA30 analyzer (Scienta Omicron AB, Uppsala, Sweden). The monochromatic X-ray of XPS and the ultraviolet light source of ARPES were generated from an Al electrode excitation source (Al Kα, 1486.7 eV) and a Helium lamp with a monochromator (He I, 21.218 eV), respectively.

3. Results and Discussion

The lattice structure of $\sqrt{3}$-Sn/Si(111) surface is illustrated in Figure 1a, showing an in-plane 30° rotation and $\sqrt{3} \times \sqrt{3}$ reconstruction of a Sn layer relative to Si(111) surface. Each Sn atom is back-bonded to three Si atoms beneath, with a remaining dangling bond at the surface. Figure 1b presents the lattice structure of T-phase $SnSe_2$ (T-$SnSe_2$). As a typical MX_2 of PTMCs, single layer T-$SnSe_2$ consists of two layers of chalcogenides and a layer of transition metal sandwiched between them, presenting a Se-Sn-Se sandwich-like structure. Within the layer, covalent bonding is achieved through Se-Sn, while interlayer stacking is achieved through Se-Se van der Waals interactions, presenting the lattice constants as $\boldsymbol{a} = 3.81$ Å and $\boldsymbol{c} = 6.14$ Å [21].

 doi:10.20944/preprints202505.0608.v1

Figure 1c-e present the RHEED patterns of an annealed Si(111)-(7×7) surface, a $\sqrt{3}$-Sn/Si(111) surface and a ML $SnSe_2$ film along the Si$[1\bar{1}0]$ direction, respectively. Corresponding RHEED patterns along the Si$[\bar{1}\bar{1}2]$ direction are also obtained by 30° rotating the sample in-plane, as shown in Figure 1f-h. From Figure 1c,f, we can see the clearly (7×7) reconstructed patterns of annealed Si surface, which are disappeared and displaced by a new pair of (1×1) diffraction stripes after the $\sqrt{3}$-Sn passivation , as shown in Figure 1d,g. Subsequently, from the Figure 1e,h, we can see the new (1×1) diffraction stripes from epitaxial $SnSe_2$ film, which are very clear and sharp, implying the high-quality crystallization.

By performing Lorentz fittings on the corresponding RHEED patterns, we can accurately obtain the (1×1) main diffraction stripe spacings of both substrates and the $SnSe_2$ films (see Figure S1 of the Supplementary Materials for details), on which we can conduct more detailed analysis and calculations. The orientation of the $\sqrt{3}$-Sn buffer layer is in-plane rotated by 30° relative to the Si(111), with the calculated lattice constant as $\boldsymbol{a}_{\sqrt{3}-\mathrm{Sn}} = 6.66 \pm 0.05$ Å, approximately equal to $\sqrt{3}$ times of $\boldsymbol{a}_{\mathrm{Si}(111)} = 3.84$ Å. This result is consistent with the previous reports [22,23]. Subsequently, the epitaxial $SnSe_2$ film is rotated by 30° again relative to $\sqrt{3}$-Sn/Si surface, resulting in the same in-plane orientation with the Si(111) substrate. Furthermore, the in-plane lattice constant of ML $SnSe_2$ is also obtained as $\boldsymbol{a}_{\mathrm{SnSe_2}} = 3.83 \pm 0.05$ Å, which is in agreement with the previous report [21].

After growth, we utilized the in-situ STM to investigate the surface morphology of ML $SnSe_2$ grown on $\sqrt{3}$-Sn/Si(111), as shown in Figure 1i. Different from three-dimensional island growth mode on graphene substrates [24], the $SnSe_2$ grown on $\sqrt{3}$-Sn/Si(111) tends to be layer-by-layer growth mode, which provides the better film flatness. The different growth modes of $SnSe_2$ on two substrates may be attributed to the larger local density of states of $\sqrt{3}$-Sn/Si(111) than that of graphene substrate, leading to an increased interface adsorption ability [25,26]. The height of ML $SnSe_2$ is ~0.62 Å [Figure 1j], which is consistent with the previous report [21].

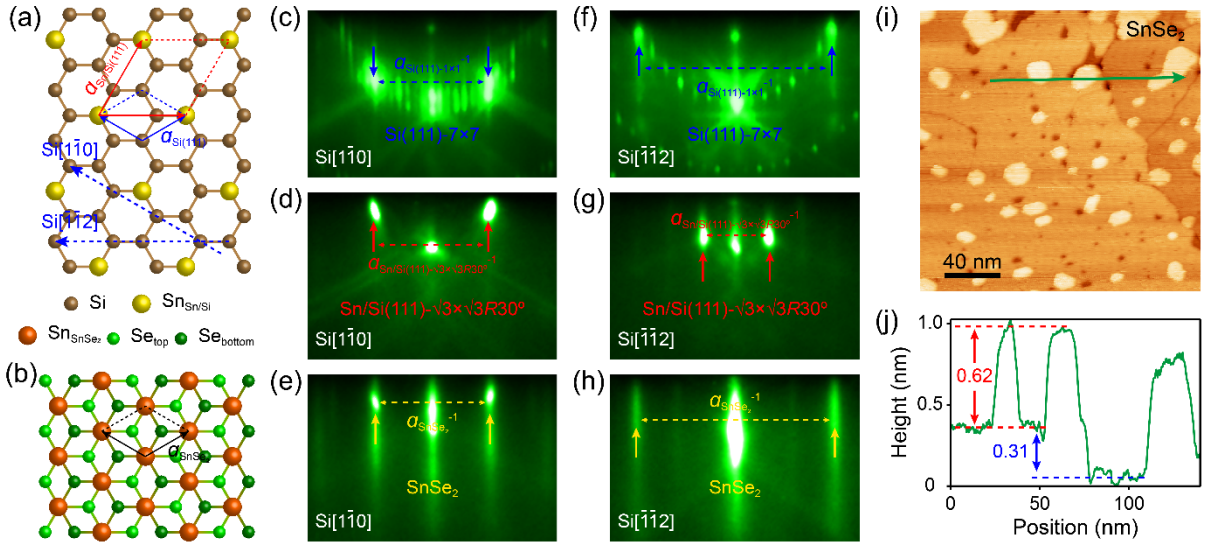

Figure 1. a) Top-view lattice structure of $\sqrt{3}$-Sn/Si(111) reconstruction. **(b)** Top-view lattice structure of a ML T-$SnSe_2$. **(c-e)** RHEED patterns of (c) Si(111)-(7×7) surface, (d) $\sqrt{3}$-Sn/Si(111) surface and (e) ML $SnSe_2$ film along the Si$[\bar{1}10]$ direction, respectively. **(f-h)** RHEED patterns of (f) Si(111)-(7×7) surface, (g) $\sqrt{3}$-Sn/Si(111) surface and (h) ML $SnSe_2$ film along the Si$[\bar{1}\bar{1}2]$ direction, respectively. **(i, j)** (i) STM topography of ML $SnSe_2$ film and (j) the corresponding height profiles along the green line in (i).

Having determined the lattice structure, we then investigated the chemical states of the $SnSe_2$ film via in-situ XPS. The full XPS spectra of Si(111), $\sqrt{3}$-Sn/Si(111) and $SnSe_2$ are shown in the Supplementary Materials Figure S2. Figure 2a presents the Si 2*p* core-level spectra of the Si(111)-(7×7) surface, $\sqrt{3}$-Sn/Si(111) and ML $SnSe_2$ film. For Si(111)-(7×7) surface, the core levels of Si $2p_{1/2}$ and Si $2p_{3/2}$ orbitals are located at 99.7 eV and 99.1 eV, in accordance with the previous literature [27]. The

 doi:10.20944/preprints202505.0608.v1

peaks red-shift by about 0.1 eV compared to the core levels of Si $2p_{1/2}$ (99.6 eV) and Si $2p_{3/2}$ (99.0 eV) orbitals of the $\sqrt{3}$-Sn/Si(111), indicating a charge transfer effect from Sn to Si upon the surface Sn-Si bond formation, which is reasonable since the electronegativity of Si is stronger than that of Sn. Besides, after the growth of ML $SnSe_2$, the core levels of Si $2p_{1/2}$ (99.8 eV) and Si $2p_{3/2}$ (99.2 eV) again shift toward higher binding energies, which suggests interfacial charge transfer from $\sqrt{3}$-Sn/Si(111) substrate to ML $SnSe_2$.

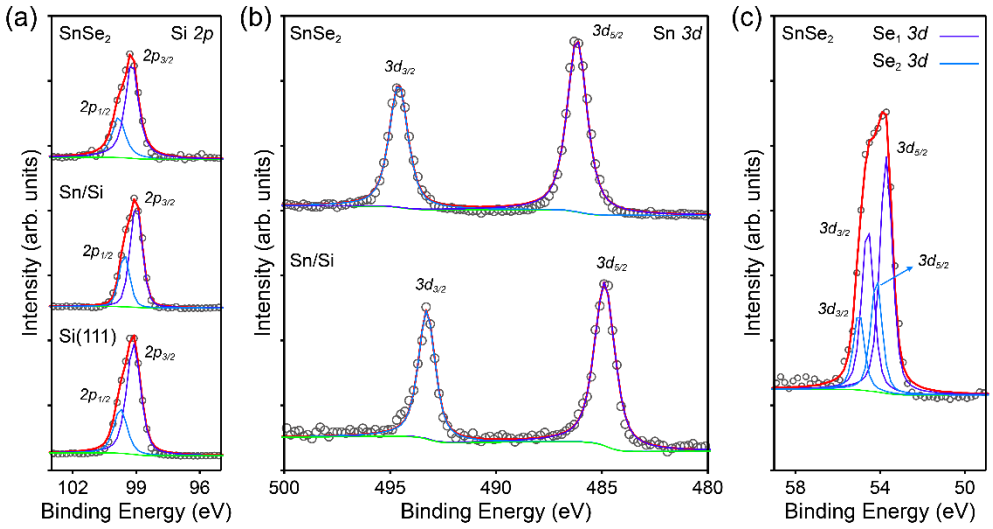

Figure 2. (a) XPS spectra around Si 2*p* orbitals of the Si(111)-(7×7) surface, $\sqrt{3}$-Sn/Si(111), and ML $SnSe_2$. **(b)** XPS spectra around Sn 3*d* orbitals of the $\sqrt{3}$-Sn/Si(111) and ML $SnSe_2$. **(c)** XPS spectra around Se 3*d* orbitals of the ML $SnSe_2$.

Subsequently, in Figure 2b, the core levels of Sn $3d_{3/2}$ (493.3 eV) and $3d_{5/2}$ (484.9 eV) orbitals of $\sqrt{3}$-Sn/Si(111) exhibit obvious blue-shift compared to the core levels of Sn $3d_{3/2}$ (494.6 eV) and $3d_{5/2}$ (486.2 eV) orbitals of ML $SnSe_2$. This shift can be explained by the much stronger bond polarity of Sn-Se than that of Sn-Si, which leads to the weakened screening to the Coulomb potential created by the positive core of Sn, and finally resulting in the higher binding energies of the remaining electrons. Besides, in Figure 2c the core levels of Se 3*d* orbitals of ML $SnSe_2$ split into two sets, Se_1 $3d_{3/2}$ (54.6 eV), Se_1 $3d_{5/2}$ (53.7 eV) and Se_2 $3d_{3/2}$ (55.0 eV), Se_2 $3d_{5/2}$ (54.2 eV), respectively. The splitting of Se 3*d* orbitals implies the presence of two nonequivalent chemical environments of Se atoms in ML $SnSe_2$. This can be attributed to that the bottom layer of Se atoms is adjacent to √3-Sn surface, while the top layer of Se atoms is located at the top surface of $SnSe_2$.

To further investigate the interface effect, we characterized the electronic structures of $SnSe_2$/$\sqrt{3}$-Sn/Si(111) system via in-situ ARPES. Figure 3 shows the electronic structures of Si(111)-(7×7) and $\sqrt{3}$-Sn/Si(111) surface. The constant energy mappings near the Fermi level of the Si(111)-(7×7) and $\sqrt{3}$-Sn/Si(111) surface clearly display the six-fold symmetry and the relative 30° rotation with respect to each other [Figure 3b,c], in accordance with the corresponding schematic of Brillouin zone (BZ) illustrated in Figure 3(a). The band structure of Si(111)-(7×7) surface is shown in Figure 3d, with the intensity enhanced zoom-in spectra plotted at the bottom panel of Figure 3e for more detailed observation. Three surface states marked as S_1, S_2 and S_3 can be clearly observed, in agreement with the previous literature [28]. The S_3 is induced by the back bonds of the (7×7) reconstruction, showing the obvious band dispersion with its maximum located at about −1.8 eV. The nearly flat S_2, induced by the rest-atoms, is located at about −0.9 eV, while the S_1, induced by the adatoms of the surface reconstruction, lying near the Fermi level.

The band structure of $\sqrt{3}$-Sn/Si(111) surface and its zoom-in spectra with enhanced intensity are plotted in Figure 3f and the top panel of Figure 3e, respectively. The surface states S_2' is located at −1~−2 eV, and the minimum of surface states S_1' is located at −0.7 eV. The S_2' and S_1' are attributed to

 doi:10.20944/preprints202505.0608.v1

the three back bonds with Si and the one remaining dangling bond of each Sn adatom, respectively [29,30]. Our results indicate the well processed substrate, on which the $SnSe_2$ films can be grown with high-quality of flatness and crystallization.

Finally, we investigated the electronic structures of $SnSe_2$ films grown on $\sqrt{3}$-Sn/Si(111) surface, as shown in Figure 4. Recent first-principles calculations and ARPES study of $SnSe_2$ showed that bulk $SnSe_2$ possesses an indirect band gap of ~1.07 eV, whose conduction band minimum (CBM) and valence band maximum (VBM) are located along the M-L and Γ-M (K) directions, respectively [31,32]. In contrast, ML $SnSe_2$ film exhibits an indirect band gap of ~1.69 eV, with CBM and VBM located at the M and Γ points, respectively [32]. The increased band gap of ML $SnSe_2$ is attributed to quantum confinement of electrons in quasi-2D samples and the reduction of the screening. The CBM of both ML and bulk $SnSe_2$ are higher than Fermi level, making it difficult to be characterized directly via ARPES in pristine $SnSe_2$.

Figure 4a is the constant energy mapping taken near the Fermi level of ML $SnSe_2$, presenting clear sixfold symmetry, with electron pockets centered at the M points of BZ. It is quite similar to that of the potassium(K)-doped $SnSe_2$ single crystals, suggesting the charge transfer from the $\sqrt{3}$-Sn/Si(111) substrate to the grown $SnSe_2$ film. Besides, the CBM of different layers of $SnSe_2$ are obtained from energy distribution curve (EDC) fittings, as shown in Figure S3. It can be clearly seen that all the CBM features appear near the Fermi level at the M point, shifting from −199 meV in ML $SnSe_2$ to −112 meV in few-layer (FL) $SnSe_2$ (the thickness of FL $SnSe_2$ is estimated to be ~3 ML), and finally to the edge of the Fermi level in multi-layer (Multi-L, the estimated thickness is about ~6 ML) $SnSe_2$ [Figure 4i-k]. The upward shift of CBM with the increase of layers again confirms the interfacial charge transfer scenario.

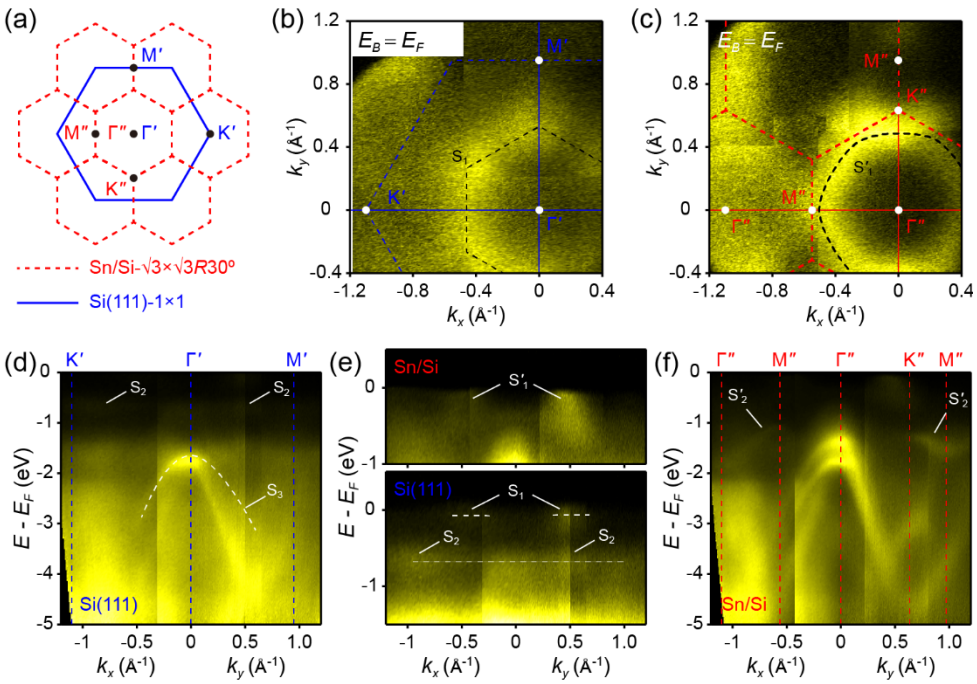

Figure 3. (a) Schematic illustration of the 2D BZs of Si(111)-(1×1) (blue solid line) and $\sqrt{3}$-Sn/Si(111) (red dashed lines) surfaces. **(b)&(c)** Constant energy mappings taken near the Fermi level of (b) Si(111) and (c) $\sqrt{3}$-Sn/Si(111) surface, respectively. The blue and red dashed lines indicate the BZs of Si(111) and $\sqrt{3}$-Sn/Si(111). **(d)** ARPES spectra of Si(111) along the K′-Γ′-M′ direction. **(e)** Zoom-in ARPES spectra near the Fermi level of $\sqrt{3}$-Sn/Si(111) (upper panel) and Si(111) (bottom panel). **(f)** ARPES spectra of $\sqrt{3}$-Sn/Si(111) along the Γ″-M″-Γ″-K″-M″ direction.

Furthermore, the ARPES spectra of ML, FL and Mult-L $SnSe_2$ along the Γ-M direction are plotted in Figure 4b-d, respectively. The VBM are all located at the Γ point. For more detailed observation, the zoom-in ARPES spectra near the VBM around the Γ point and corresponding EDCs along the red

 doi:10.20944/preprints202505.0608.v1

lines are illustrated in Figure 4e-g,h. Intriguingly, we note that a new band α above the original VBM of bulk $SnSe_2$ emerges in the ML and FL $SnSe_2$ films, which disappears in the Mult-L $SnSe_2$. The emerging α band can be better resolved in the second-derivative spectra, as shown in Figure S4. From the EDC fittings in Figure 4h, the maximum of the α band is located at −1.05 eV and −0.97 eV in ML and FL $SnSe_2$, respectively, leading to the reduced band gaps as 0.85 eV in both of them. The position as well as the relatively flat dispersion of α band are quite similar to the top valence band of H phase $SnSe_2$ (H-$SnSe_2$), which was characterized and marked as '7/8' band in a previous literature [33]. Moreover, a recent first-principle calculation showed a reduced band gap of H-$SnSe_2$ compared to T-$SnSe_2$, in accordance with our ARPES results[34]. Therefore, we believe that the newly emerged energy band α would be attributed to the presence of a small amount of H-$SnSe_2$ formed in ML and FL $SnSe_2$. Indeed, a pressure induced structural phase transition to H-$SnSe_2$ was reported before[35]. Therefore, we assume that the interfacial strain from $\sqrt{3}$-Sn/Si(111) substrate would be the main reason for the emergence of H-$SnSe_2$, which vanishes gradually as the film become thicker. Furthermore, the indistinct band structures of ML and FL $SnSe_2$, contrary to the clear band structures in Multi-L $SnSe_2$, also provides evidence for our assumption, since the band structures of both T-$SnSe_2$ and H-$SnSe_2$ can be detected by ARPES and eventually overlap together in the spectra, as shown in Figure 4b,c.

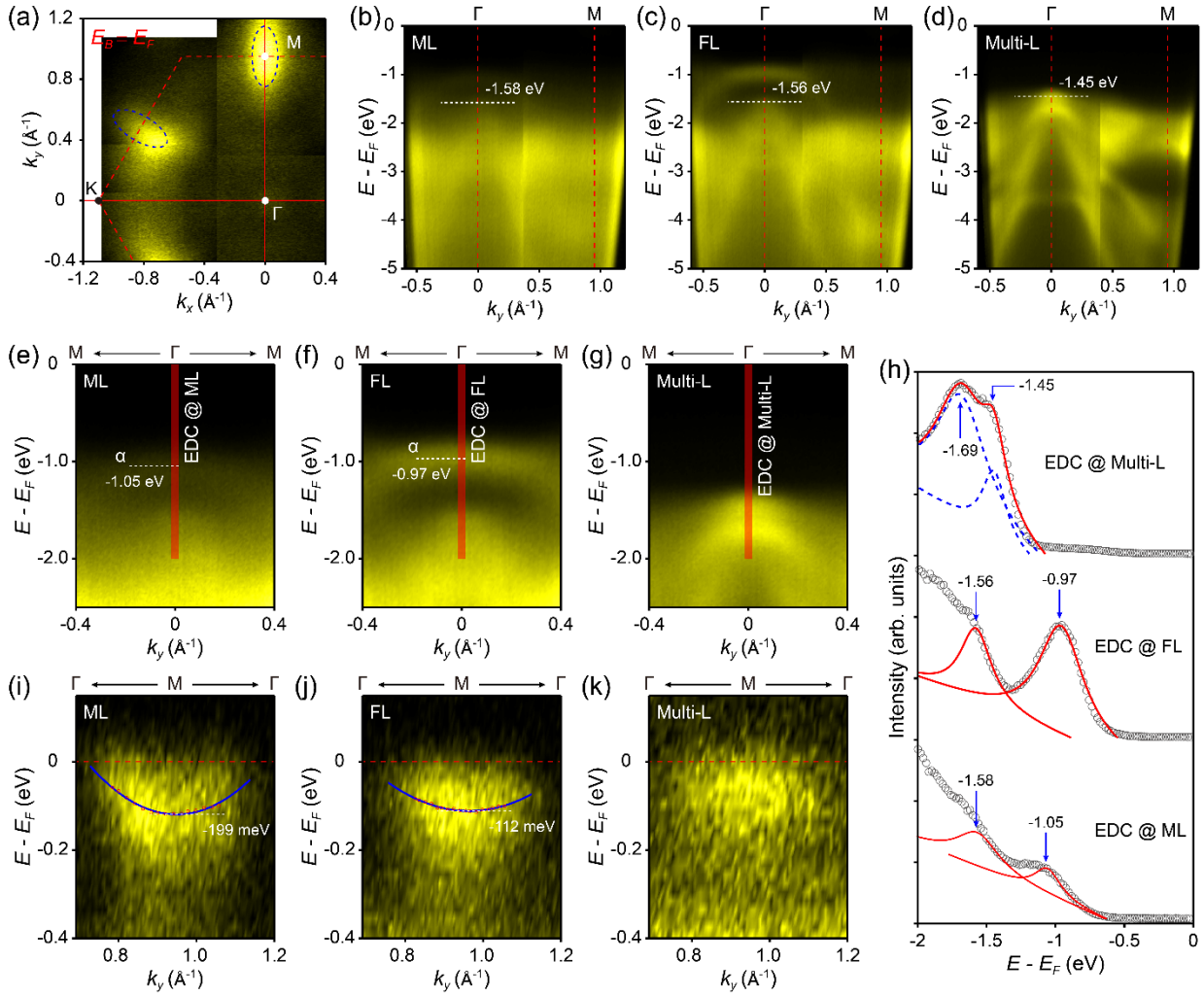

Figure 4. (a) Constant energy mapping taken near the Fermi level of ML $SnSe_2$. The red dashed lines indicate the 2D BZ of $SnSe_2$. **(b-d)** ARPES spectra of (b) ML, (c) FL and (d) Multi-L $SnSe_2$ along the Γ-M direction, respectively. **(e-g)** Zoom-in ARPES spectra near the VBM of (e) ML, (f) FL and (g) Multi-L $SnSe_2$ around the Γ point. **(h)** EDCs along the red lines in (e-g). The red curves are the Lorentzian fittings to the EDCs. **(i-k)** Zoom-in ARPES spectra near the CBM of (i) ML, (j) FL and (k) Multi-L $SnSe_2$ around the M point, respectively.

 doi:10.20944/preprints202505.0608.v1

4. Conclusions

In summary, we have realized the MBE growth of $SnSe_2$ films on $\sqrt{3}$-Sn passivated Si(111) substrate. The analysis of RHEED patterns demonstrate the successful growth and the same in-plane lattice orientation of the grown $SnSe_2$ with Si(111) substrate, whereas the Sn buffer layer conducts a $(\sqrt{3} \times \sqrt{3})$ reconstruction with in-plane rotation by 30° relative to both Si(111) and $SnSe_2$. Besides, the layer-by-layer growth mode of $SnSe_2$ identified by STM indicates the relatively strong adsorption effect of $\sqrt{3}$-Sn/Si(111) on $SnSe_2$ adsorbates. Subsequently, from the XPS measurements, we observed the interfacial charge transfer from substrate to $SnSe_2$, which was further confirmed in the ARPES measurements. Moreover, a new valence band $\boldsymbol{\alpha}$ located above the original VBM of bulk $SnSe_2$ emerges in the ML and FL $SnSe_2$ films, which disappears in the Multi-layer $SnSe_2$ film. We attribute it to the partial T→H structural phase transition of thin $SnSe_2$ films grown on $\sqrt{3}$-Sn/Si(111) substrate, probably driven by the interfacial strain. The direct characterizations of electronic structures of $SnSe_2$ films, as well as the layer-dependent structural transition, along with the effective band modulation, provide significant and important information for the further applications of $SnSe_2$ films in 2D electronic devices.

Supplementary Materials: The following supporting information can be downloaded at the website of this paper posted on Preprints.org., A. Method for calculating lattice constants from RHEED patterns; B. Full XPS spctra; C. EDCs fitting for determining the CBMs; D. Second-derivative ARPES spectra.

Author Contributions: Conceptualization, Y.Z.; methodology, Z.L., Q.T., K.W., Y.M., Z.F., X.Q., Q.M., C.W., and Y.Z.; software, Y.Z.; validation, Z.L., Q.T., K.W., Y.M. and Y.Z.; formal analysis, Z.L., Q.T., K.W., Y.M. and Y.Z.; investigation, Z.L. and Q.T.; resources, Y.Z.; data curation, Z.L., Q.T., K.W., Y.M. and Y.Z.; writing—original draft preparation, Z.L.; writing—review and editing, Y.Z.; visualization, Z.L., Q.T., K.W. and Y.M.; supervision, C.W. and Y.Z.; project administration, Y.Z.; funding acquisition, Y.Z.. All authors have read and agreed to the published version of the manuscript.

Funding: This research was funded by the National Natural Science Foundation of China (No. 92165205), the Fundamental Research Funds for the Central University (No. 0204/14380228), the Fundamental Research Program of Natural Science Foundation of Jiangsu Province (BK20243011), and the Natural Science Foundation of Hunan Province of China (No. 2024jj6009).

Institutional Review Board Statement: Not applicable.

Informed Consent Statement: Not applicable.

Data Availability Statement: Dataset available on request from the authors.

Conflicts of Interest: The authors declare no conflicts of interest.

Abbreviations

The following abbreviations are used in this manuscript:

PTMCs	Post-transition metal dichalcogenides
CDW	Charge density wave
ML	Monolayer
MBE	Molecular beam epitaxy
RHEED	Reflection high energy electron diffraction
XPS	X-ray photoemission spectroscopy
ARPES	Angle-resolved photoemission spectroscopy
UHV	Ultra-high-vacuum
BZ	Brillouin zone
CBM	Conduction band minimum
VBM	Valence band maximum
EDC	Energy distribution curve

 doi:10.20944/preprints202505.0608.v1

FL	Few-layer
Multi-L	Multi-layer

References

1 Tan, S. M.; Chua, C. K.; Sedmidubský, D.; Sofer, Z. B., and Pumera, M.; Electrochemistry of layered GaSe and GeS: Applications to ORR, OER and HER *Physical Chemistry Chemical Physics* **2016**, 18, 1699.

2 Wang, Y.; Szökölová, K.; Nasir, M. Z. M.; Sofer, Z., and Pumera, M.; Electrochemistry of Layered Semiconducting $A^{III}B^{VI}$ Chalcogenides: Indium Monochalcogenides (InS, InSe, InTe) *ChemCatChem* **2019**, 11, 2634.

3 Sucharitakul, S.; Goble, N. J.; Kumar, U. R.; Sankar, R.; Bogorad, Z. A.; Chou, F. C.; Chen, Y. T., and Gao, X. P. A.; Intrinsic Electron Mobility Exceeding 103 cm2/(V s) in Multilayer InSe FETs *Nano Letters* **2015**, 15, 3815.

4 Xu, K.; Yin, L.; Huang, Y.; Shifa, T. A.; Chu, J.; Wang, F.; Cheng, R.; Wang, Z., and He, J.; Synthesis, properties and applications of 2D layered $M^{III}X^{VI}$ (M = Ga, In; X = S, Se, Te) materials *Nanoscale* **2016**, 8, 16802.

5 Sucharitakul, S.; Goble, N. J.; Kumar, U. R.; Sankar, R.; Bogorad, Z. A.; Chou, F.-C.; Chen, Y.-T., and Gao, X. P. A.; Intrinsic Electron Mobility Exceeding 10^3 $cm^2/(Vs)$ in Multilayer InSe FETs *Nano Letters* **2015**, 15, 3815.

6 Hu, P.; Wen, Z.; Wang, L.; Tan, P., and Xiao, K.; Synthesis of few-layer GaSe nanosheets for high performance photodetectors *ACS Nano* **2012**, 6, 5988.

7 Hu, P.; Zhang, J.; Yoon, M.; Qiao, X.-F.; Zhang, X.; Feng, W.; Tan, P.; Zheng, W.; Liu, J.; Wang, X.; Idrobo, J. C.; Geohegan, D. B., and Xiao, K.; Highly sensitive phototransistors based on two-dimensional GaTe nanosheets with direct bandgap *Nano Research* **2014**, 7, 694.

8 Marvan, P.; Mazánek, V., and Sofer, Z.; Shear-force exfoliation of indium and gallium chalcogenides for selective gas sensing applications *Nanoscale* **2019**, 11, 4310.

9 Li, G.; Ding, G., and Gao, G.; Thermoelectric properties of $SnSe_2$ monolayer *Journal of Physics: Condensed Matter* **2017**, 29, 015001.

10 Shafique, A.; Samad, A., and Shin, Y.-H.; Ultra low lattice thermal conductivity and high carrier mobility of monolayer SnS_2 and $SnSe_2$: a first principles study *Physical Chemistry Chemical Physics* **2017**, 19, 20677.

11 Huang, Y.; Xu, K.; Wang, Z.; Shifa, T. A.; Wang, Q.; Wang, F.; Jiang, C., and He, J.; Designing the shape evolution of $SnSe_2$ nanosheets and their optoelectronic properties *Nanoscale* **2015**, 7, 17375.

12 Zhou, X.; Gan, L.; Tian, W.; Zhang, Q.; Jin, S.; Li, H.; Bando, Y.; Golberg, D., and Zhai, T.; Ultrathin $SnSe_2$ Flakes Grown by Chemical Vapor Deposition for High-Performance Photodetectors *Advanced Materials* **2015**, 27, 8035.

13 Luo, Y.; Zheng, Y.; Luo, Z.; Hao, S.; Du, C.; Liang, Q.; Li, Z.; Khor, K. A.; Hippalgaonkar, K.; Xu, J.; Yan, Q.; Wolverton, C., and Kanatzidis, M. G.; n-Type $SnSe_2$ Oriented-Nanoplate-Based Pellets for High Thermoelectric Performance *Advanced Energy Materials* **2018**, 8, 1702167.

14 Choi, J.; Jin, J.; Jung, I. G.; Kim, J. M.; Kim, H. J., and Son, S. U.; $SnSe_2$ nanoplate–graphene composites as anode materials for lithium ion batteries *Chemical Communications* **2011**, 47, 5241.

15 Wang, R. Y.; Caldwell, M. A.; Jeyasingh, R. G. D.; Aloni, S.; Shelby, R. M.; Wong, H. S. P., and Milliron, D. J.; Electronic and optical switching of solution-phase deposited $SnSe_2$ phase change memory material *Journal of Applied Physics* **2011**, 109, 113506.

16 Zhang, Y.-M.; Fan, J.-Q.; Wang, W.-L.; Zhang, D.; Wang, L.; Li, W.; He, K.; Song, C.-L.; Ma, X.-C., and Xue, Q.-K.; Observation of interface superconductivity in a $SnSe_2$ epitaxial graphene van der Waals heterostructure *Physical Review B* **2018**, 98, 220508.

17 Mao, Y.; Ma, X.; Wu, D.; Lin, C.; Shan, H.; Wu, X.; Zhao, J.; Zhao, A., and Wang, B.; Interfacial Polarons in van der Waals Heterojunction of Monolayer $SnSe_2$ on SrTiO3 (001) *Nano Letters* **2020**, 20, 8067.

18 Wang, S.-Z.; Zhang, Y.-M.; Fan, J.-Q.; Ren, M.-Q.; Song, C.-L.; Ma, X.-C., and Xue, Q.-K.; Charge density waves and Fermi level pinning in monolayer and bilayer $SnSe_2$ *Physical Review B* **2020**, 102, 241408.

19 Wu, H.; Li, S.; Susner, M.; Kwon, S.; Kim, M.; Haugan, T., and Lv, B.; Spacing dependent and cation doping independent superconductivity in intercalated 1T 2D $SnSe_2$ *2D Materials* **2019**, 6, 045048.

 doi:10.20944/preprints202505.0608.v1

20 Zeng, J.; Liu, E.; Fu, Y.; Chen, Z.; Pan, C.; Wang, C.; Wang, M.; Wang, Y.; Xu, K.; Cai, S.; Yan, X.; Wang, Y.; Liu, X.; Wang, P.; Liang, S.-J.; Cui, Y.; Hwang, H. Y.; Yuan, H., and Miao, F.; Gate-Induced Interfacial Superconductivity in 1T-$SnSe_2$ *Nano Letters* **2018**, 18, 1410.

21 Schlüter, M. and Cohen, M. L.; Valence-band density of states and chemical bonding for several non-transition-metal layer compounds: $SnSe_2$, PbI_2, BiI_3, and GaSe *Physical Review B* **1976**, 14, 424.

22 Zhachuk, R. A.; Rogilo, D. I.; Petrov, A. S.; Sheglov, D. V.; Latyshev, A. V.; Colonna, S., and Ronci, F.; Atomic structure of a single step and dynamics of Sn adatoms on the Si(111)-√3×√3-Sn surface *Physical Review B* **2021**, 104, 125437.

23 Wu, X.; Ming, F.; Smith, T. S.; Liu, G.; Ye, F.; Wang, K.; Johnston, S., and Weitering, H. H.; Superconductivity in a Hole-Doped Mott-Insulating Triangular Adatom Layer on a Silicon Surface *Physical Review Letters* **2020**, 125, 117001.

24 Zhang, Y.; Wang, C.; Tian, Q.; Meng, Q.; Zong, J., and Zhang, Y.; Epitaxial Growth of Monolayer $SnSe_2$ Films on Gd-Intercalated Quasi-Free-Standing Monolayer Graphene with Enhanced Interface Adsorption *The Journal of Physical Chemistry C* **2022**, 126, 5751.

25 Jiang, P.; Ma, X.; Ning, Y.; Song, C.; Chen, X.; Jia, J.-F., and Xue, Q.-K.; Quantum Size Effect Directed Selective Self-Assembling of Cobalt Phthalocyanine on Pb(111) Thin Films *Journal of the American Chemical Society* **2008**, 130, 7790.

26 Huttmann, F.; Martínez-Galera, A. J.; Caciuc, V.; Atodiresei, N.; Schumacher, S.; Standop, S.; Hamada, I.; Wehling, T. O.; Blügel, S., and Michely, T.; Tuning the van der Waals Interaction of Graphene with Molecules via Doping *Physical Review Letters* **2015**, 115, 236101.

27 Barr, T. L.; An XPS study of Si as it occurs in adsorbents, catalysts, and thin films *Applications of Surface Science* **1983**, 15, 1.

28 Sheverdyaeva, P. M.; Mahatha, S. K.; Ronci, F.; Colonna, S.; Moras, P.; Satta, M., and Flammini, R.; Signature of surface periodicity in the electronic structure of Si(1 1 1)-(7 × 7) *Journal of physics. Condensed matter : an Institute of Physics journal* **2017**, 29, 215001.

29 Kinoshita, T.; Kono, S., and Sagawa, T.; Angle-resolved photoelectron-spectroscopy study of the Si(111) √3×√3-Sn surface: Comparison with Si(111) √3×√3-Al, -Ga, and -In surfaces *Physical Review B* **1986**, 34, 3011.

30 Lobo, J.; Tejeda, A.; Mugarza, A., and Michel, E. G.; Electronic structure of Sn/Si(111)-√3×√3*R*30° as a function of Sn coverage *Physical Review B* **2003**, 68, 235332.

31 Lochocki, E. B.; Vishwanath, S.; Liu, X.; Dobrowolska, M.; Furdyna, J.; Xing, H. G., and Shen, K. M.; Electronic structure of $SnSe_2$ films grown by molecular beam epitaxy *Applied Physics Letters* **2019**, 114, 091602.

32 Gonzalez, J. M. and Oleynik, I. I.; Layer-dependent properties of ${\mathbf{SnS}}_{2}$ and ${\mathbf{SnSe}}_{2}$ two-dimensional materials *Physical Review B* **2016**, 94, 125443.

33 Bertrand, Y.; Solal, F., and Levy, F.; Experimental band structure of 2H-$SnSe_2$ by synchrotron radiation photoemission spectroscopy *Journal of Physics C: Solid State Physics* **1984**, 17, 2879.

34 Brizolla, G. M. S.; Chaves, A. J.; Teles, L. K.; Guilhon, I., and Junior, J. M. P.; Electrically controlled charge qubit in van der Waals heterostructures: From ab initio calculation to tight-binding models *Physical Review B* **2024**, 109, 125416.

35 Ge, B.; Li, C.; Lu, W.; Ye, H.; Li, R.; He, W.; Wei, Z.; Shi, Z.; Kim, D.; Zhou, C.; Zhu, M.; Wuttig, M., and Yu, Y.; Dynamic Phase Transition Leading to Extraordinary Plastic Deformability of Thermoelectric $SnSe_2$ Single Crystal *Advanced Energy Materials* **2023**, 13, 2300965.